Temperature Sensitivity of ^{14}N-V and ^{15}N-V Ground-State Manifolds

Sean Lourette,[1,2,*] Andrey Jarmola,[1,2] Victor M. Acosta,[3] A. Glen Birdwell,[2] Dmitry Budker,[1,4,5] Marcus W. Doherty,[6] Tony Ivanov,[2] and Vladimir S. Malinovsky[2]

[1] *Department of Physics, University of California, Berkeley, California 94720, USA*
[2] *DEVCOM Army Research Laboratory, Adelphi, Maryland 20783, USA*
[3] *Center for High Technology Materials, and Department of Physics and Astronomy, University of New Mexico, Albuquerque, New Mexico 87106, USA*
[4] *Johannes Gutenberg-Universität Mainz, Mainz 55128, Germany*
[5] *Helmholtz-Institut, GSI Helmholtzzentrum für Schwerionenforschung, Mainz 55128, Germany*
[6] *Department of Quantum Science & Technology, Research School of Physics, Australian National University, Canberra 2601, Australia*

(Received 22 December 2022; revised 3 May 2023; accepted 15 May 2023; published 30 June 2023)

We measure electron- and nuclear-spin transition frequencies in the ground state of nitrogen-vacancy (N-V) centers in diamond for two nitrogen isotopes (^{14}N-V and ^{15}N-V) over temperatures ranging from 77 to 400 K. Measurements are performed using Ramsey interferometry and direct optical readout of the nuclear and electron spins. We extract coupling parameters Q (for ^{14}N-V), D, $A_\parallel$, $A_\perp$, and γ_e/γ_n, and their temperature dependences for both isotopes. The temperature dependences of the nuclear-spin transitions within the $m_s = 0$ spin manifold near room temperature are found to be 0.52(1) ppm/K for ^{14}N-V ($|m_I = -1\rangle \leftrightarrow |m_I = +1\rangle$) and $-1.1(1)$ ppm/K for ^{15}N-V ($|m_I = -1/2\rangle \leftrightarrow |m_I = +1/2\rangle$). An isotopic shift in the zero-field splitting parameter D between ^{14}N-V and ^{15}N-V is measured to be ~ 120 kHz. Residual transverse magnetic fields are observed to shift the nuclear-spin transition frequencies, especially for ^{15}N-V. We have precisely determined the set of parameters relevant for the development of nuclear-spin-based diamond quantum sensors with greatly reduced sensitivity to environmental factors.

DOI: 10.1103/PhysRevApplied.19.064084

I. INTRODUCTION

In recent years, color centers in diamond, and, in particular, the nitrogen-vacancy (N-V) center, have emerged as one of the key platforms for quantum-technology applications, particularly in sensing [1]. As the technology matures, detailed knowledge of the parameters of the system and their environmental dependence become a prerequisite for development of accurate devices such as magnetometers, gyroscopes, clocks, as well as multisensors. For nitrogen-vacancy-based rotation sensing [2–4], one may use ^{14}N-V and ^{15}N-V centers, where using two isotopes is important for differential measurements to separate rotational, magnetic, and temperature effects [5–10].

In this work, which follows the earlier experimental studies of the temperature dependence of the ground-state zero-field splitting parameter D [11], the electric quadrupole hyperfine splitting parameter Q [12], and the theoretical analysis [13], we present a complete experimental characterization of the temperature dependence of the coupling parameters of N-V centers for both nitrogen isotopes (^{14}N-V and ^{15}N-V), including the dependence of the magnetic hyperfine coupling parameters $A_\parallel$ and $A_\perp$. We find that N-V parameters are generally temperature-dependent, with relative sensitivity ranging from 7 to 90 ppm/K at room temperature, depending on the parameter.

Additional findings of this work include identification of the relatively high sensitivity of ^{15}N-V nuclear-spin levels to misalignment of the magnetic field to the N-V axis, as well as measurement of the isotopic shift in D at a level of ~ 40 ppm. The latter is important for testing the theoretical models of the system in order to attain a level of understanding necessary for accurate modeling of devices. Note that ^{15}N-V nuclear spins were recently explored as a resource for quantum sensing not relying on microwave (MW) or radio-frequency (rf) fields in Ref. [14].

*slourette@berkeley.edu

II. THEORETICAL BACKGROUND

The Hamiltonian for the electronic ground state of ^{14}N-V and ^{15}N-V [15] is given by

$$H = DS_z^2 + QI_z^2 + A_\parallel S_z I_z + \gamma_e B\, S_z - \gamma_n B\, I_z + \frac{A_\perp}{2}\left(S_+ I_- + S_- I_+\right), \tag{1}$$

where D is the ground-state zero-field splitting parameter of the N-V center, Q is the nuclear electric quadrupole parameter (only for ^{14}N-V), $A_\parallel$ and $A_\perp$ are the longitudinal and transverse magnetic hyperfine coupling parameters (see Table II for parameter values at 297 K), γ_e is the gyromagnetic ratio of the N-V center (2.8033(3) MHz/G [16]), γ_n is the gyromagnetic ratio of the nitrogen nuclear spin ($^{14}\gamma_n = 307.59(3)$ Hz/G and $^{15}\gamma_n = -431.50(4)$ Hz/G), **B** is the external magnetic field applied along the z axis (N-V symmetry axis), and **S** and **I** are electron- and nuclear-spin operators, respectively. In Eq. (1), we neglect the transverse components of the magnetic field $B = \|\mathbf{B}\|$.

The energy-level diagrams for the electronic ground states of ^{14}N-V and ^{15}N-V are shown in Fig. 1. The electron-spin transitions $|m_s = 0\rangle \leftrightarrow |m_s = \pm 1\rangle$ are labeled as $f_\pm^{(m_I)}$, where m_I denotes the nuclear-spin state. The ^{14}N-V and ^{15}N-V nuclear-spin transitions are labeled f_1 to f_6 and f_7 to f_9, respectively, according to the diagram. The nuclear-spin double-quantum transition with frequency $f_1 - f_2$ is labeled as f_{DQ} and is of particular interest for rotation sensing [17,18] and comagnetometry [19,20].

Nuclear-spin transition frequencies for both ^{14}N-V and ^{15}N-V can be derived using perturbation theory (see Appendix C), and are described to lowest order in $A_\perp/(D \pm \gamma_e B)$ by the following expressions:

$$\begin{aligned}
f_1 &\approx |Q| + {}^{14}\gamma_n B - \frac{A_\perp^2}{D - \gamma_e B},\\
f_2 &\approx |Q| - {}^{14}\gamma_n B - \frac{A_\perp^2}{D + \gamma_e B},\\
f_3 &\approx |Q| - |A_\parallel| + {}^{14}\gamma_n B,\\
f_4 &\approx |Q| + |A_\parallel| - {}^{14}\gamma_n B + \frac{A_\perp^2}{D - \gamma_e B},\\
f_5 &\approx |Q| + |A_\parallel| + {}^{14}\gamma_n B + \frac{A_\perp^2}{D + \gamma_e B},\\
f_6 &\approx |Q| - |A_\parallel| - {}^{14}\gamma_n B,
\end{aligned} \tag{2}$$

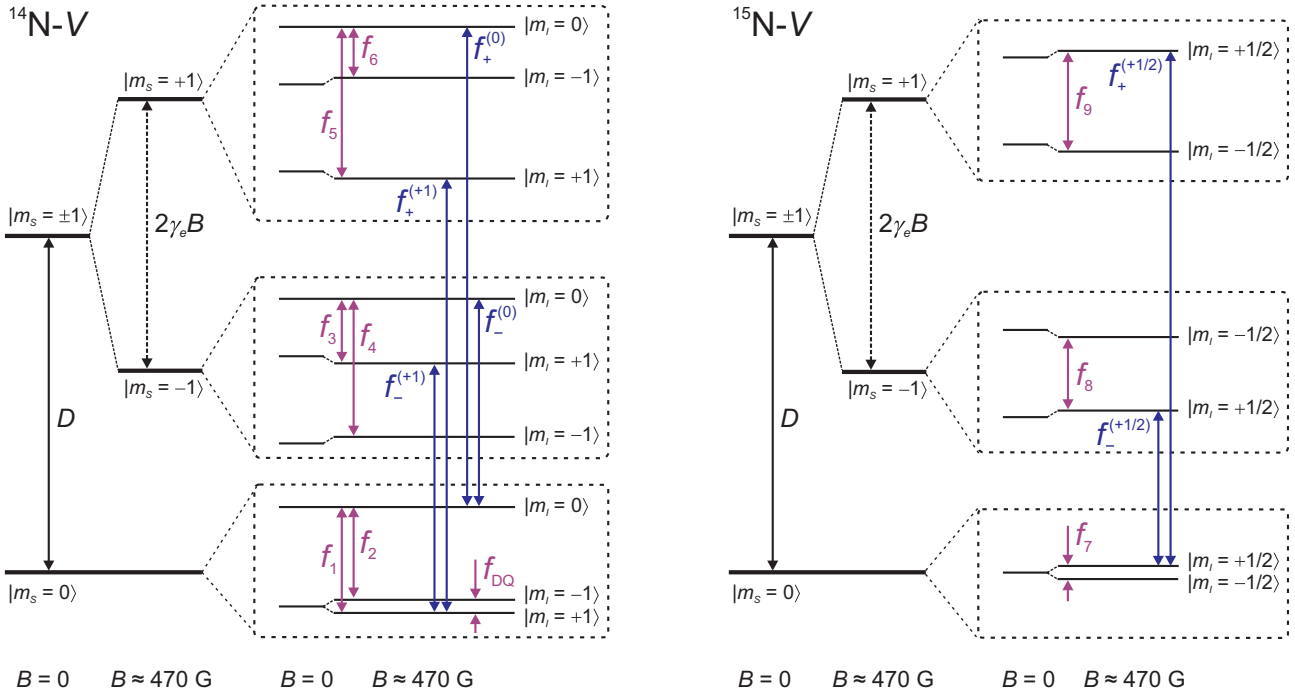

FIG. 1. Energy-level diagrams for the electronic ground states of ^{14}N-V and ^{15}N-V. Energy levels are described by electron-spin (m_s) and nuclear-spin (m_I) quantum numbers. The electron-spin transitions used in this experiment are shown with blue arrows, and are labeled as $f_\pm^{(m_I)}$ for $|m_s = 0\rangle \leftrightarrow |m_s = \pm 1\rangle$, where m_I denotes the nuclear-spin state of the transition. The nuclear-spin transitions are shown with purple arrows, and are labeled f_1 to f_9. The energy-level diagrams are depicted for the magnetic field values shown at the bottom.

and

$$f_7 \approx |^{15}\gamma_n|B + \frac{A_\perp^2}{2}\left(\frac{1}{D-\gamma_e B} - \frac{1}{D+\gamma_e B}\right),$$
$$f_8 \approx A_\parallel - |^{15}\gamma_n|B - \frac{A_\perp^2}{2}\left(\frac{1}{D-\gamma_e B}\right),$$
$$f_9 \approx A_\parallel + |^{15}\gamma_n|B - \frac{A_\perp^2}{2}\left(\frac{1}{D+\gamma_e B}\right). \quad (3)$$

In this work, the transition frequencies f_1 to f_9, $f_\pm^{(+1)}$, and $f_\pm^{(+1/2)}$ are measured in the presence of an axial field ($B \approx 470$ G) at temperatures ranging from 77 to 400 K.

III. EXPERIMENTAL METHODS

We used a custom-built epifluorescence microscopy setup (as in Ref. [17]) to measure optically detected magnetic resonances (ODMRs) in an ensemble of N-V centers. Four diamond samples, whose properties are listed in Table I, were used in our experiments: two with natural isotopic ratio of nitrogen, and two with enhanced ^{15}N concentration.

The diamond sample was mounted inside a continuous-flow microscopy cryostat (Janis ST-500). A bias magnetic field B (470–480 G) was applied along one of the N-V axes using two temperature-compensated samarium-cobalt (Sm_2Co_{17} grade: EEC 2:17-TC16) ring magnets, which were arranged in a Helmholtz-like configuration that minimizes magnetic field gradients across the detected volume. An aspheric condenser lens with a numerical aperture of 0.79 was used to illuminate a ~ 50 μm spot on the diamond with ~ 30 mW of 532 nm laser light and collect fluorescence. The N-V sensing volume is $\sim 10^{-3}$ mm^3, defined by the area of the incident laser beam and the length of its path through the diamond. The fluorescence was separated from the excitation light by a dichroic mirror, passed through a band-pass filter (650 to 800 nm), and detected by a free-space Si photodiode. MW and rf signals were delivered using a 160-μm-diameter copper wire placed on the diamond surface next to the optical focus. The generation of MW and rf signals is described in detail in the supplemental information section of Ref. [17].

The transition frequencies of the N-V ground state were measured with Ramsey interferometry using pulse sequences that are shown in Fig. 2(a). For each nuclear-spin transition frequency (f) between a pair of states ($|m_s, m_I\rangle$ and $|m_s, m_I'\rangle$), the following steps are performed: optical polarization, state preparation, Ramsey interferometry, and optical readout. Polarization is done with a green laser pulse with duration 100–200 μs, which polarizes the electron and nuclear spins into $|0,+1\rangle$ (or $|0,+1/2\rangle$ for ^{15}N-V) [12,21–23]. State $|m_s, m_I\rangle$ is prepared by transferring population using a sequence of rf and MW π pulses. Next, a superposition of the states $|m_s, m_I\rangle$ and $|m_s, m_I'\rangle$ is created using a Ramsey $\pi/2$ pulse with frequency $f_{\rm rf}$ (duration 10–100 μs). The superposition then accumulates a phase at a rate given by the detuning frequency, $\delta = f_{\rm rf} - f$ (typically 0.5–10 kHz). After a variable delay time τ, the acquired relative phase is projected into a population difference with a second $\pi/2$ pulse and read out optically. Direct optical readout of the nuclear-spin state is performed without the use of microwave mapping pulses, which is possible at magnetic fields near the excited-state level anticrossing [12]. To determine f, we obtain δ by fitting the Ramsey oscillations with an exponentially decaying sinusoidal function. Measurements of electron-spin transition frequencies (f_+, f_-) were performed in the same way, using MW pulses instead of rf pulses. Figure 2(b) shows an example of a Ramsey measurement for the nuclear transition frequency f_1.

IV. RESULTS

The transition frequencies of ^{14}N-V (f_1 to f_6, $f_+^{(+1)}$, and $f_-^{(+1)}$) and ^{15}N-V (f_7 to f_9, $f_+^{(+1/2)}$, and $f_-^{(+1/2)}$) were measured using the previously described Ramsey interferometry technique [Figs. 2(a) and 2(b)] in the presence of an axial magnetic field $B \approx 470$ G for temperatures ranging from 77 to 400 K using four samples; see Table I. For each temperature, the system was allowed to equilibrate for several hours, after which we sequentially measured each of the transition frequencies of electron spins, then nuclear spins, and then electron spins again. This was done in order to ensure the temperature drift was sufficiently small during the $\sim$ 30-minute measurement period.

TABLE I. Diamond samples. The estimated concentrations of substitutional nitrogen [N], N-V centers [N-V], and ^{13}C atoms [^{13}C], in addition to the nitrogen isotopic ratio [^{14}N]:[^{15}N], electron-spin dephasing time T_2^*, and electron-spin coherence time T_2, are listed for each sample used in experiments. Millimeter-sized bulk diamonds were grown using chemical vapor deposition and were obtained from Element Six. Electron-spin T_2^* was measured using Ramsey interferometry, and T_2 was measured using Hahn echo techniques.

Sample	[N] (ppm)	[N-V] (ppm)	[^{14}N]:[^{15}N]	[^{13}C] (%)	T_2^* (μs)	T_2 (μs)
F7	~ 0.1	~ 0.01	99.6:0.4	1.1	1.8(2)	600(20)
G2	10	4	99.6:0.4	<0.01	1.0(2)	11(1)
M1	~ 10	~ 1	20:80	...	0.25(2)	15(2)
G3	16	4.5	50:50	1.1	0.35(3)	22(2)

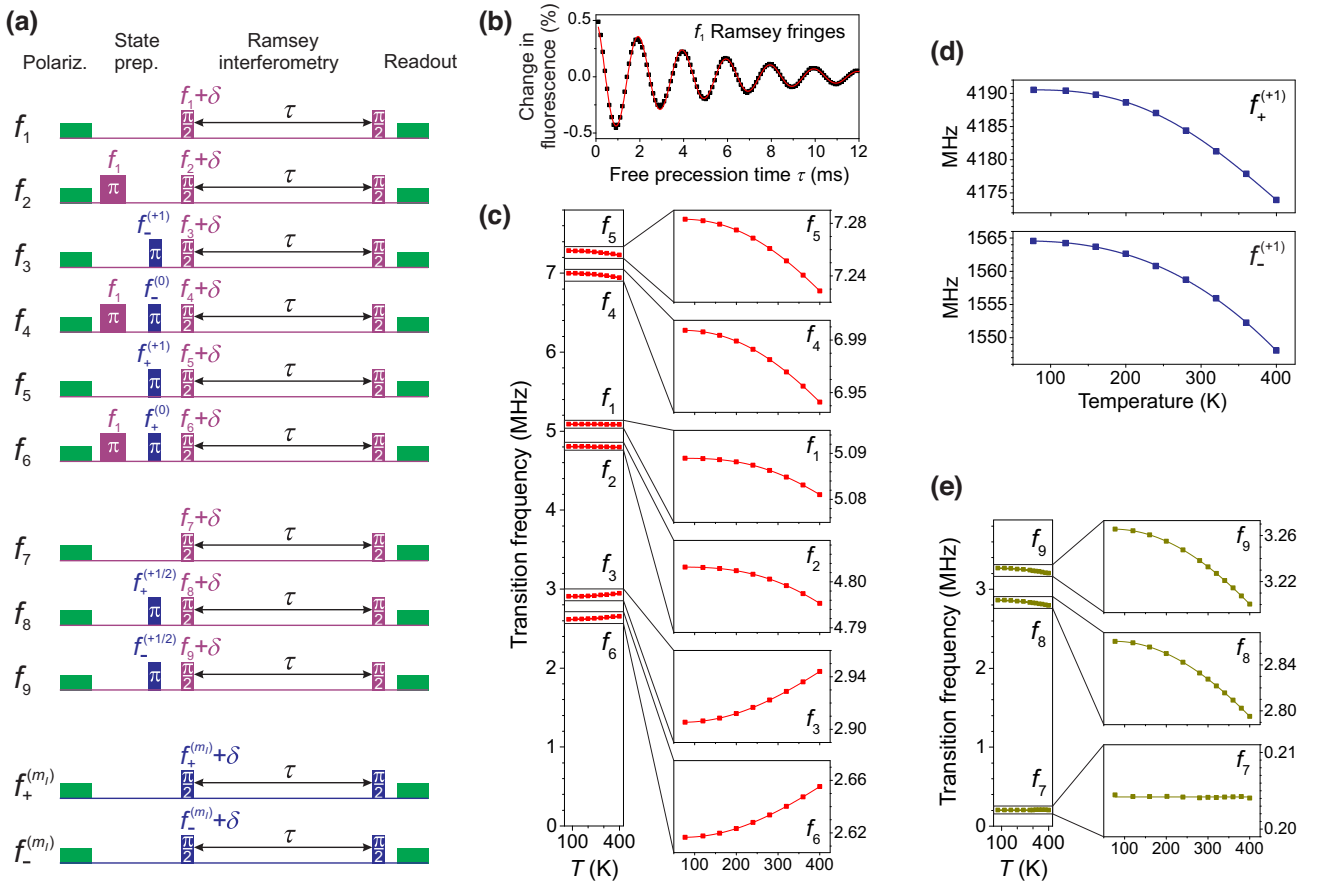

FIG. 2. Ramsey measurements of ground-state transition frequencies. (a) Nuclear-spin transition frequencies f_1 to f_6 (^{14}N-V) and f_7 to f_9 (^{15}N-V) as well as electron-spin transition frequencies f_+ and f_- for both isotopes are measured using Ramsey interferometry. After optical polarization (green) with green light, the nuclear spin is manipulated with a series of rf (purple) and MW (blue) pulses to prepare a superposition of the two relevant energy states. The superposition then precesses at the detuning frequency δ for a variable time τ, after which a $\pi/2$ rf pulse converts the acquired phase into a population difference to be read out optically. (b) Example of the nuclear Ramsey interferometry measurement. The oscillation frequency of the Ramsey fringes corresponds to the detuning δ from the transition frequency f_1. (c) Temperature dependence of f_1 to f_6 for sample G2 at $B \approx 470$ G. The y-axis range for the f_1 and f_2 subplots has been reduced (70 kHz $\rightarrow$ 20 kHz) to show the reduced temperature dependence of f_1 and f_2. (d) Temperature dependence of f_+ and f_- for ^{14}N-V (^{15}N-V not shown) for sample G2 at $B \approx 470$ G. (e) Temperature dependence of f_7 to f_9 for sample M1 at $B \approx 468$ G. The y-axis range for the f_7 subplot has been reduced (80 kHz $\rightarrow$ 12 kHz).

Figures 2(c) and 2(d) show the temperature dependence of the nuclear-spin and electron-spin transitions in ^{14}N-V for sample G2. Transition frequencies f_1 and f_2 are least sensitive to temperature, varying by 8 kHz across the range, while f_3, f_6 and f_4, f_5 vary by ~ 40 kHz and ~ 50 kHz, respectively. These temperature dependences are largely determined by the temperature dependence of Q and $A_\parallel$, according to Eq. (2). Figure 2(e) shows the temperature dependence of the nuclear-spin transitions in ^{15}N-V for sample M1, which has been isotopically enriched with ^{15}N. Transition frequencies f_8 and f_9 were measured to vary by ~ 70 kHz across the measured range of temperatures, while the temperature dependence of f_7 was found to be three orders of magnitude smaller; see Sec. V for detailed analysis.

Using all measured transition frequencies, we apply the numerical methods described in Appendix A to extract values for the coupling parameters for both ^{14}N-V (D, Q, $A_\parallel$, $A_\perp$, and $\gamma_e/^{14}\gamma_n$) and ^{15}N-V (D, $A_\parallel$, $A_\perp$, and $\gamma_e/^{15}\gamma_n$).

Numerically extracted coupling parameters for ^{14}N-V (D, Q, $A_\parallel$, and $A_\perp$) and ^{15}N-V (D and $A_\parallel$) are plotted as a function of temperature in Figs. 3(a)–3(e). Each parameter's temperature dependence was fitted to a fourth-order polynomial. Figure 3(f) shows the fractional shift of each parameter as a function of temperature. We observe ^{14}N-V and ^{15}N-V to have identical fractional dependence for both D and $A_\parallel$.

In the case of $A_\perp$ for ^{15}N-V, the following factors prevented the determination of its temperature dependence: (i) $A_\perp$ has a weak contribution to the nuclear-spin transition

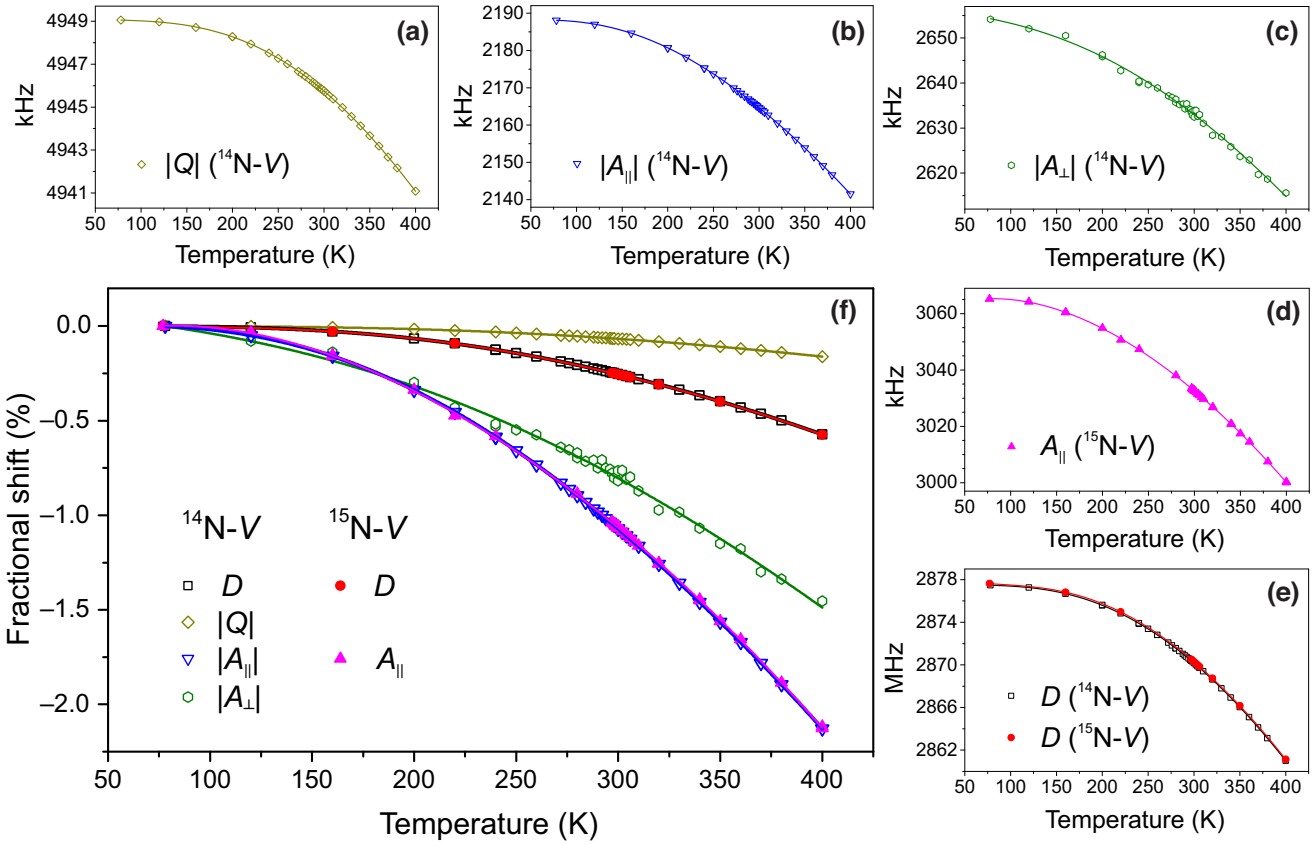

FIG. 3. Temperature dependence of coupling parameters. (a)–(e) Coupling parameters D, Q, $A_\parallel$, and $A_\perp$ were extracted numerically (see Appendix A) from measured nuclear-spin and electron-spin transition frequencies. Coupling parameters are plotted against temperature, for both ^{14}N-V and ^{15}N-V, using data from all diamond samples. The solid lines are fourth-degree polynomial fits. (f) Fractional temperature dependence of all parameters whose data are presented in panels (a)–(e). In those, ^{14}N-V and ^{15}N-V were found to have similar fractional temperature shifts in D and in $A_\parallel$.

frequencies; (ii) the ^{15}N-V nuclear-spin transition frequencies (f_7 in particular) are sensitive to magnetic field misalignment θ (see Sec. V A); and (iii) ^{15}N-V has only three nuclear-spin transitions, whose frequencies are determined by four parameters, i.e., $A_\parallel$, $A_\perp$, $^{15}\gamma_n B$, and θ. We were able to overcome these issues at room temperature by scanning the transverse magnetic field with coils [see Fig. 5(c)] and obtained $A_\perp = 3.68(2)$ MHz, which is in agreement with Ref. [16]. In future studies, this approach can be used to obtain the temperature dependence of ^{15}N-V $A_\perp$.

Table II lists the values and temperature derivatives of each coupling parameter at 297 K for both ^{14}N-V and ^{15}N-V, obtained from the polynomial fits. The room-temperature value for each measured parameter is

TABLE II. Experimentally determined coupling parameters at 297 K. The values and temperature derivatives of coupling parameters ^{14}N-V (D, Q, $A_\parallel$, and $A_\perp$) and ^{15}N-V (D and $A_\parallel$) at 297 K are obtained from the polynomial fits of the temperature dependences shown in Fig. 3. The $A_\perp$ value for ^{15}N-V is obtained by scanning the transverse magnetic field with coils; see Fig. 5(c).

Isotope	Parameter	Value (kHz)	First derivative (Hz/K)	Fractional derivative (ppm/K)	Second derivative (Hz/K^2)
^{14}N-V	D	$2870.28(3) \times 10^3$	$-72.5(5) \times 10^3$	$-25.3(2)$	$-0.39(1) \times 10^3$
	Q	$-4945.88(1)$	$35.5(3)$	$-7.17(6)$	$0.22(1)$
	$A_\parallel$	$-2165.19(8)$	$197(1)$	$-91.0(5)$	$0.73(6)$
	$A_\perp$	$-2635(2)$	$154(5)$	$-58(2)$	$0.53(3)$
^{15}N-V	D	$2870.38(3) \times 10^3$	$-72(1) \times 10^3$	$-25.1(3)$	$-0.40(2) \times 10^3$
	$A_\parallel$	$3033.3(1)$	$-269(3)$	$-89(1)$	$-0.98(8)$
	$A_\perp$	$3680(20)$			

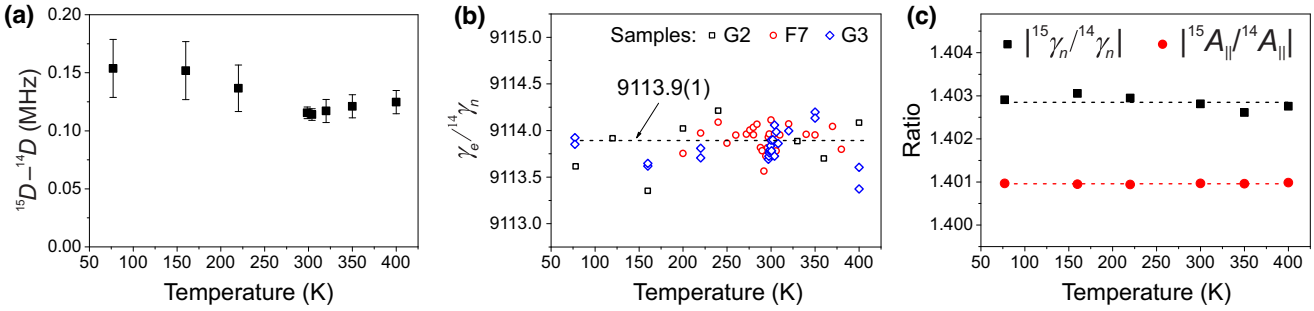

FIG. 4. Temperature-insensitive parameters. (a) Difference in the zero-field splitting parameter D between ^{14}N-V and ^{15}N-V. (b) Ratio of electron-spin gyromagnetic ratio γ_e and ^{14}N-V nuclear-spin gyromagnetic ratio $^{14}\gamma_n$. (c) Isotopic ratios of γ_n and of $A_\parallel$ for ^{14}N-V and ^{15}N-V. Markers are experimental data, and dashed lines are mean values. In panels (a) and (c), the data were measured using sample G3, which has a 50:50 ratio of [^{15}N-V]:[^{14}N-V]. The error bars were determined from the reproducibility of the results.

consistent with previously reported values [16,22–24]. Temperature derivatives are also consistent with previously reported values for ^{14}N-V parameters D [11,25,26], Q [12,26–28], and $A_\parallel$ [26–28]. Recent theoretical work [29] provided *ab initio* evaluation of the temperature dependences of several parameters for the ^{14}N-V system. In the cases where the same parameters were calculated in Ref. [29] and measured here, we find good agreement. The temperature derivatives for ^{14}N-V $A_\perp$ and ^{15}N-V $A_\parallel$ are reported here for the first time.

We observe an isotopic shift of $\sim$ 120 kHz ($\sim$ 40 ppm) in the D parameter, with D larger for ^{15}N-V. Figure 4(a) shows the shift in D across the full range of measured temperatures for the G3 sample, which has a 50:50 isotopic ratio (grown with evenly mixed ^{14}N and ^{15}N). This effect is also clearly visible as a difference in separation of peaks in the ODMR signal (see Appendix B). The relatively small isotopic effect in D is in line with the fact that even a replacement of the species adjacent to the vacancy changes the zero-field splitting only slightly; see recent work [30], where the D values were reported to be 2888 MHz and 2913 MHz for the O-V^0 and B-V^-, respectively.

Figure 4(b) shows the numerically extracted values of $\gamma_e/^{14}\gamma_n$ for three different samples. The mean value of $\gamma_e/^{14}\gamma_n$ is measured to be 9113.9(1), which is in agreement with Ref. [31]. Using the literature value for $\gamma_e = 2.8033(3)$ MHz/G [16], this corresponds to $^{14}\gamma_n = 307.59(3)$ Hz/G. The value for $\gamma_e/^{14}\gamma_n$ can also be approximated without numerical methods from the measured frequencies directly [see Eq. (2)]:

$$\frac{\gamma_e}{^{14}\gamma_n} \approx \frac{f_+^{(0)} - f_-^{(0)}}{f_3 - f_6} \approx \frac{f_+^{(+1)} - f_-^{(+1)} + f_5 - f_3}{f_3 - f_6}. \quad (4)$$

Figure 4(c) shows the isotopic ratio of γ_n ($|^{15}\gamma_n/^{14}\gamma_n| = 1.40285(6)$, in agreement with Ref. [32]) and the isotopic ratio of $A_\parallel$ ($|^{15}A_\parallel/^{14}A_\parallel| = 1.40096(1)$) obtained from measurements using the G3 sample. The difference in these ratios can be used to verify theoretical models. When using the literature value for γ_e, we obtain $^{15}\gamma_n = -431.50(4)$ Hz/G.

V. DISCUSSION

A. Temperature and angular dependences of f_{DQ} and f_7

The nuclear-spin transitions f_{DQ} and f_7 within the $m_s = 0$ manifold of ^{14}N-V and ^{15}N-V are of particular interest for sensing applications such as rotation sensing [17,18] and comagnetometry [19,20]. Precise knowledge of their transition frequencies and their dependence on environmental factors (temperature, magnetic field) is essential for optimal sensor performance. The transition frequencies f_{DQ} and f_7 can be obtained from Eqs. (2) and (3) and are described by the following expressions:

$$f_{DQ} \approx 2 \times {}^{14}\gamma_n B \left(1 - \left|\frac{\gamma_e}{^{14}\gamma_n}\right| \frac{A_\perp^2}{D^2 - \gamma_e^2 B^2}\right), \quad (5)$$

$$f_7 \approx |^{15}\gamma_n| B \left(1 + \left|\frac{\gamma_e}{^{15}\gamma_n}\right| \frac{A_\perp^2}{D^2 - \gamma_e^2 B^2}\right). \quad (6)$$

The frequencies of these transitions do not depend on the coupling parameters Q and $A_\parallel$, and are determined primarily by the nuclear Zeeman shift $\Delta m_I \gamma_n B$, resulting in a greatly reduced temperature dependence compared to other nuclear-spin transitions. Therefore, measurements of the temperature dependences of f_{DQ} and f_7 require more precise control of the bias magnetic field.

Over the range of temperatures used in this experiment, the bias magnetic field varied by $\sim$ 1 G, primarily due to thermal expansion of the sample holder in the presence of magnetic field gradients. This variation in the bias magnetic field was measured using electron-spin transition frequencies and subsequently used to obtain corrected values for f_{DQ} and f_7 corresponding to 480 G. When the temperature is changed from 77 to 400 K, the corrected values of f_{DQ} and f_7 are observed to shift by 140 ppm

(44 Hz at 480 G) and −260 ppm (−55 Hz at 480 G), respectively; see Fig. 5(a). This corresponds to fractional temperature derivatives of 0.52(1) ppm/K (0.15 Hz/K) for f_{DQ} and −1.1(1) ppm/K (−0.10 Hz/K) for f_7 at 297 K.

The temperature dependences of f_{DQ} and f_7 arise from the temperature dependence of $A_\perp^2/D^2$ and are described by Eqs. (5) and (6). These equations are used with experimentally obtained polynomial fits of $A_\perp$ and D (see Fig. 3) to generate the solid and dashed lines in Fig. 5(a). For f_7, $A_\perp$ is assumed to have the same fractional dependence on temperature as $A_\parallel$. For sufficiently small fields $\gamma_e B \ll D$ (i.e., $B = 10$ G), the transition frequencies are approximately linear in the magnetic field, and thus the fractional shift is independent of magnetic field.

Magnetic field misalignment (from the N-V axis) is another factor that can significantly shift the transition frequencies of f_{DQ} and f_7, and must be considered in sensing applications. Angular-dependent shifts in f_7 are significantly stronger than shifts in f_{DQ} because of the lack of a stabilizing coupling parameter (i.e., Q) in the effective nuclear-spin Hamiltonian. The frequency shifts f_{DQ} and f_7 exhibit a quadratic dependence on misalignment angle, and are shown in Figs. 5(b) and 5(c), respectively. The alignment of the magnetic field was controlled using two pairs of coils oriented perpendicular to the bias magnetic field B_z. The transverse magnetic field B_x was precisely determined using the N-V electron-spin transitions of the three nonaxial N-V subensembles. We measure a frequency shift of 5.0 Hz in f_{DQ} and of 130 Hz in f_7 when misaligning the magnetic field by $\theta = 0.1^\circ$ ($B_x \approx 0.8$ G) at a field of $B_z = 480$ G.

We use numerical methods (Appendix A) together with experimental values from Table II to obtain theoretical predictions for the angular dependence of f_{DQ} and f_7 at 480 G (solid line) and 10 G (dashed line). For f_7, we fit the theoretical model to the experimental data in order to obtain a more precise value of $A_\perp$ for ^{15}N-V, which we measure to be 3.68(2) MHz at 297 K.

The frequency shifts in f_{DQ} and f_7 due to magnetic field misalignment can be approximated using perturbation theory; see Appendix C. For f_{DQ} the dominant term is a second-order correction, whose fractional shift is described by the following expression:

$$\frac{\Delta f_{DQ}}{2 \times {}^{14}\gamma_n B_z} \approx \frac{1}{2}\beta\,\theta^2,$$
$$\beta = -\frac{\gamma_e}{{}^{14}\gamma_n}\frac{4|A_\parallel| D\,\gamma_e^2 B_z^2}{(D^2 - \gamma_e^2 B_z^2)^2}, \tag{7}$$

where θ is the angle between the N-V axis and the magnetic field, and $\beta \approx -9.9$ at $B_z = 480$ G, and $\beta \approx -0.003$ at $B_z = 10$ G.

While the second-order correction is similar to that of f_{DQ}, for f_7 the fourth-order correction is much larger and is

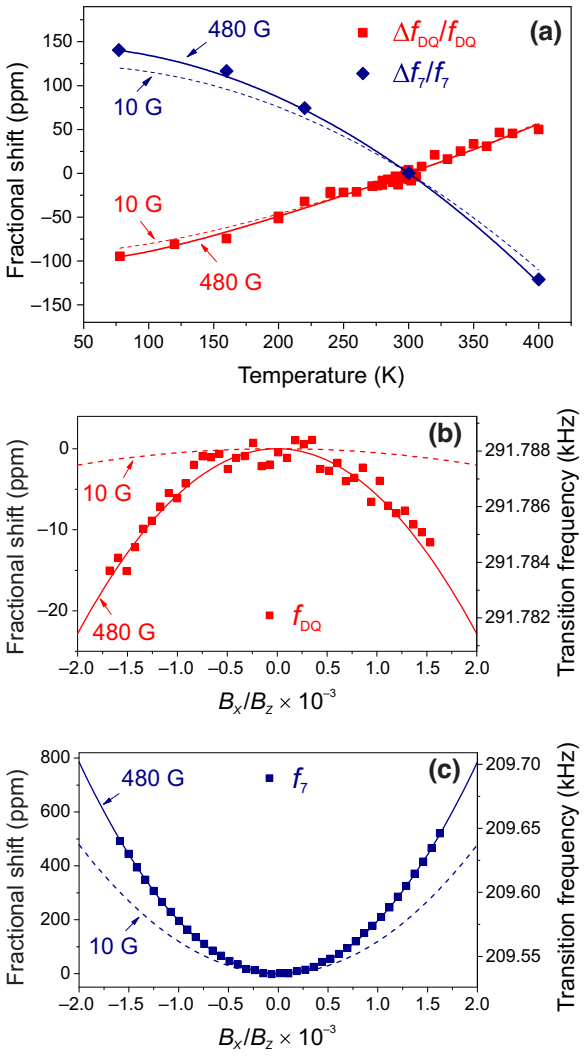

FIG. 5. Temperature and angular dependences of f_{DQ} and f_7. (a) The fractional shifts in nuclear transition frequencies f_{DQ} (red) and f_7 (blue) are plotted as a function of temperature. Markers represent experimental data after correcting for variations in the magnetic field between measurements. Solid and dashed lines were obtained from Eqs. (5) and (6) at 480 G and 10 G, respectively. (b),(c) The fractional shifts in nuclear transition frequencies f_{DQ} (red) and f_7 (blue), respectively, are plotted as a function of magnetic field misalignment with respect to the N-V axis for fixed values of B_z. Markers represent experimental data, and solid (480 G) and dashed (10 G) lines were obtained by numerically diagonalizing the Hamiltonian [Eq. (1)] using values from Table II. For f_7 in panel (c), $A_\perp$ is treated as a free parameter, and fit to the experimental data in order to obtain $A_\perp = 3.68(2)$ MHz.

described by the following expression:

$$\frac{\Delta f_7}{{}^{15}\gamma_n B_z} \approx \frac{1}{2}\beta\,\theta^2,$$
$$\beta = \frac{\gamma_e^2}{{}^{15}\gamma_n^2}\frac{4A_\perp^2 D^2}{(D^2 - \gamma_e^2 B_z^2)^2}, \tag{8}$$

where $\beta \approx 460$ at $B_z = 480$ G, and $\beta \approx 280$ at $B_z = 10$ G.

B. Anisotropy of the hyperfine coupling

The temperature dependence of the magnetic hyperfine coupling components, $A_\parallel$ and $A_\perp$, is used to obtain the temperature dependence of the Fermi-contact and dipolar terms. These in turn can be expressed in terms of the effective spin density η occupying the atomic orbitals of the nitrogen atom and their effective hybridization ratio $|c_p|^2/|c_s|^2$ via the expressions

$$f = \frac{8\pi}{3}\frac{\mu_0}{4\pi} g_e \mu_B \mu_n |c_s|^2 \eta |\psi_s(0)|^2 = 1811 \text{ MHz} \times (1 - |c_s|^2)\eta, \quad (9)$$

$$d = \frac{2}{5}\frac{\mu_0}{4\pi} g_e \mu_B \mu_n |c_p|^2 \eta \left\langle \psi_p \left| \frac{1}{r^3} \right| \psi_p \right\rangle = 55.52 \text{ MHz} \times |c_p|^2 \eta. \quad (10)$$

Figure 6 shows that both the spin density and hybridization ratio are observed to increase with temperature. This is consistent with the *ab initio* calculations [33], which concluded that, with increasing temperature, the spin density diffuses away from the three carbon atoms surrounding the vacancy and the nitrogen atom moves towards the vacancy (away from its nearest-neighbor carbon atoms). Thus, one would expect the spin density to increase at the nitrogen atom as a result of the outward diffusion, and the displacement of the nitrogen atom would lead to an increase in the hybridization ratio (as the orbitals connecting the nitrogen to its nearest neighbors must become more p-like to achieve the new geometry of the bond).

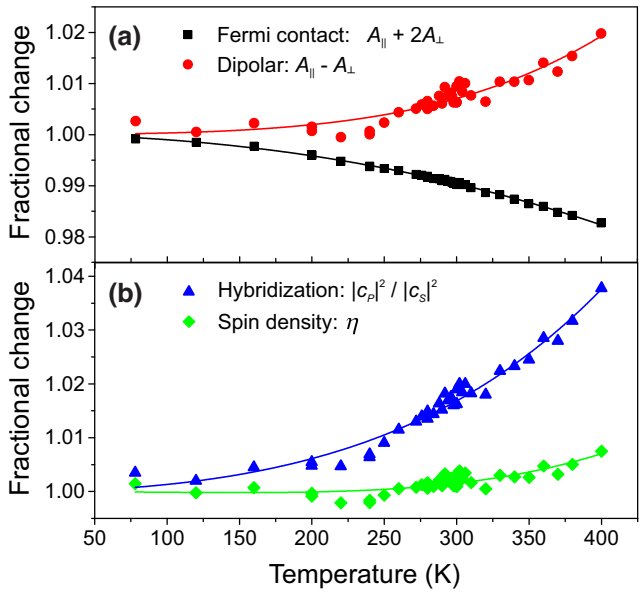

FIG. 6. Anisotropy of the ^{14}N-V magnetic hyperfine coupling. Temperature dependences of (a) the Fermi-contact ($f = A_\parallel + 2A_\perp$) and dipolar ($d = A_\parallel - A_\perp$) terms, and (b) the N-$V$ orbital hybridization $|c_p|^2/|c_s|^2$ and spin density η obtained from Eqs. (9) and (10). Markers are experimental data, and solid lines are polynomial fits.

VI. CONCLUSION AND OUTLOOK

We measured the nuclear-spin and electron-spin transition frequencies for N-V centers containing ^{14}N and ^{15}N, as a function of temperature. To describe the results, we used numerical diagonalization of the Hamiltonian, including the effect of magnetic field misalignment. The model allows us to extract the underlying parameters Q (for ^{14}N-V), D, $A_\parallel$, $A_\perp$, and γ_e/γ_n for both isotopes and their temperature dependences (except $A_\perp$ for ^{15}N-V). The magnitude of each one of these parameters (Q, D, $A_\parallel$, and $A_\perp$) decreases with temperature in the range from 77 to 400 K, showing a reduction of $\sim 0.1\%$ (in the case of Q) to $\sim 2\%$ (in the case of $A_\parallel$).

Comparison of the determined parameters reveals a difference in D of ~ 120 kHz (~ 40 ppm) between N-V centers containing ^{14}N and ^{15}N. This is the first report of such an isotopic difference for N-V centers. We also observe a difference of $\sim 0.1\%$ between $^{15}A_\parallel/^{14}A_\parallel$ and $^{15}\gamma_n/^{14}\gamma_n$.

The temperature dependence of the anisotropy of the hyperfine coupling between electron and nuclear spins ($A_\parallel$, $A_\perp$) in ^{14}N-V can be used to infer the temperature dependence of the Fermi-contact and dipolar interactions, which, in turn, can provide information about the electron-spin density and orbital hybridization.

We determined the temperature dependence of f_{DQ} (0.52(1) ppm/K) and f_7 ($-1.1(1)$ ppm/K), which are three orders of magnitude smaller than the other nuclear-spin transition frequencies. Nevertheless, this sensitivity to temperature may limit the performance of nuclear-spin-based sensors and should be taken into account.

We found that residual transverse fields should be carefully considered in order to precisely determine the frequencies, especially for f_7, for which a misalignment of the field by 0.1° leads to a fractional change of ~ 600 ppm. This strong dependence allowed us to measure $A_\perp$ for ^{15}N-V to be 3.68(2) MHz, which is in agreement with the previously measured value [16].

The combination $f_3 - f_6$ has negligible dependence on $A_\perp$ and is described to high precision by $f_3 - f_6 = 2\gamma_n B$, and therefore its temperature dependence is predicted to be weak: < 10 ppb/K.

In summary, we have precisely determined the set of parameters relevant for the development of N-V–diamond rotation sensors, magnetometers, frequency standards, and multisensors, along with the temperature dependence of these parameters. The results indicate a promising path to developing such devices with greatly reduced sensitivity to

environmental variations. The general idea is to use multiple transitions with different sensitivity to, for example, temperature, which allows one to isolate the environmental parameter drift from the effect of interest (e.g., inertial rotation).

ACKNOWLEDGMENTS

The authors are grateful to Junichi Isoya, Pauli Kehayias, and Janis Smits for helpful discussions. S.L. and A.J. acknowledge support from the U.S. Army Research Laboratory under Cooperative Agreement No. W911NF-21-2-0030 and No. W911NF-18-2-0037. V.M.A. acknowledges support from NSF Grant No. CHE-1945148, and NIH Grants No. 1R41GM145129 and No. 1DP2GM140921. This work was supported in part by the EU FET-OPEN Flagship Project ASTERIQS (action 820394) and by the European Commission's Horizon Europe Framework Program under the Research and Innovation Action MUQUABIS GA No. 101070546.

APPENDIX A: NUMERICAL METHODS – EIGENVALUES AND LEAST-SQUARES FITTING

The full ground-state Hamiltonian of ^{14}N-V (and ^{15}N-V, which is noted in parenthesis throughout this section) is

$$H = DS_z^2 + QI_z^2 + A_\parallel S_z I_z + \gamma_e B_z S_z - \gamma_n B_z I_z + \frac{A_\perp}{2}(S_+ I_- + S_- I_+) + \gamma_e B_x S_x - \gamma_n B_x I_x, \quad \text{(A1)}$$

and includes a transverse magnetic field, which is assumed without loss of generality to point in the $+x$ direction. (For ^{15}N-V, use $Q = 0$.) Given a set of values for the coupling parameters of ^{14}N-V (and ^{15}N-V), which we will denote as the vector

$$\mathbf{a} = \langle D, \gamma_e B_z, Q, A_\parallel, A_\perp, \gamma_e B_x, \gamma_e/{}^{14}\gamma_n, (D, A_\parallel, A_\perp, \gamma_e/{}^{15}\gamma_n)\rangle,$$

we can use eigenvalue decomposition to numerically obtain the nine (plus six) energy eigenvalues and therefore the frequencies of the six (plus three) rf transitions and two (plus two) MW transitions of the ground-state Hamiltonian of the ^{14}N-V center, denoted as

$$\mathbf{f}(\mathbf{a}) = \langle f_1, f_2, f_3, f_4, f_5, f_6, f_+^{(+1)}, f_-^{(+1)}, (f_7, f_8, f_9, f_+^{(+1/2)}, f_-^{(+1/2)})\rangle.$$

Here, we need to solve the inverse problem, starting with experimental values for the transition frequencies, **f**, and ending with values for the coupling parameters, **a**. This is done starting with an initial guess for the coupling parameters, $\mathbf{a}_0$, calculating the transition frequencies associated with this guess $\mathbf{f}(\mathbf{a}_0)$, and an associated weighted error between the calculated and measured transition frequencies $\mathcal{S}(\mathbf{a}) = \sum_i |(1/\delta f_i)(f_i(\mathbf{a}) - f_i)|^2$, where $\delta\mathbf{f}$ is the measurement uncertainty associated with **f**. The fitted values for the coupling parameters correspond to the value of **a** that minimizes $\mathcal{S}(\mathbf{a})$, which was obtained using MATLAB's *fminsearch* function (Nelder-Mead simplex algorithm). This process was repeated for each temperature to obtain the temperature dependence of each parameter.

TABLE III. Transition frequencies and temperature derivatives at $T = 297$ K and $B = 470$ G. Values are determined by performing numerical diagonalization of the Hamiltonian [Eq. (1)] using values and uncertainties of D, Q, $A_\parallel$, and $A_\perp$ listed in Table II. For ^{15}N-V, it is assumed that $A_\perp$ has the same fractional temperature dependence as $A_\parallel$ within 5%, or $(dA_\perp/dT)/A_\perp = 1.00(5) \times (dA_\parallel/dT)/A_\parallel$.

Parameter	Value (kHz)	Derivative (Hz/K)
f_1	5085.95(1)	−35.2(2)
f_2	4799.65(1)	−35.3(2)
f_3	2925.22(8)	161.5(7)
f_4	6970.98(8)	−232.8(7)
f_5	7257.28(8)	−232.7(7)
f_6	2636.14(8)	161.5(7)
$f_1 - f_2$	286.299(2)	0.149(8)
$f_5 - f_4$	286.299(2)	0.149(8)
$f_3 - f_6$	289.081(2)	−0.000(0)
f_7	205.89(3)	− 0.31(2)
f_8	2825.8(1)	−268(2)
f_9	3234.8(1)	−269(2)

Using the fitted temperature dependence of the coupling parameters, we numerically diagonalize the Hamiltonian at and near 297 K for $B = 470$ G. This allows us to estimate the temperature dependence of the magnetically sensitive nuclear transitions (f_1 to f_9), which are shown in Table III.

APPENDIX B: ISOTOPIC SHIFT IN D

The isotopic shift in D can be measured directly from the pulsed ODMR spectrum, which is shown in Fig. 7. Signals were recorded for the G3 sample at 475 G and 298 K. At this field, the nuclear spins are optically polarized to their largest m_I sublevels, $m_I = +1$ for ^{14}N-V and $m_I = +1/2$ for ^{15}N-V, which are individually resolvable due to the opposite signs of $^{14}\gamma_n$ and $^{15}\gamma_n$. By extracting D using $(f_+ + f_-)/2$ for each isotope, we obtain $D = 2870.26$ MHz for ^{14}N-V and $D = 2870.38$ MHz for ^{15}N-V, which correspond to an isotopic shift in the D parameter of 0.12(1) MHz.

APPENDIX C: PERTURBATION THEORY

Perturbation theory can be used to describe how both the transverse hyperfine coupling parameter ($A_\perp$) and

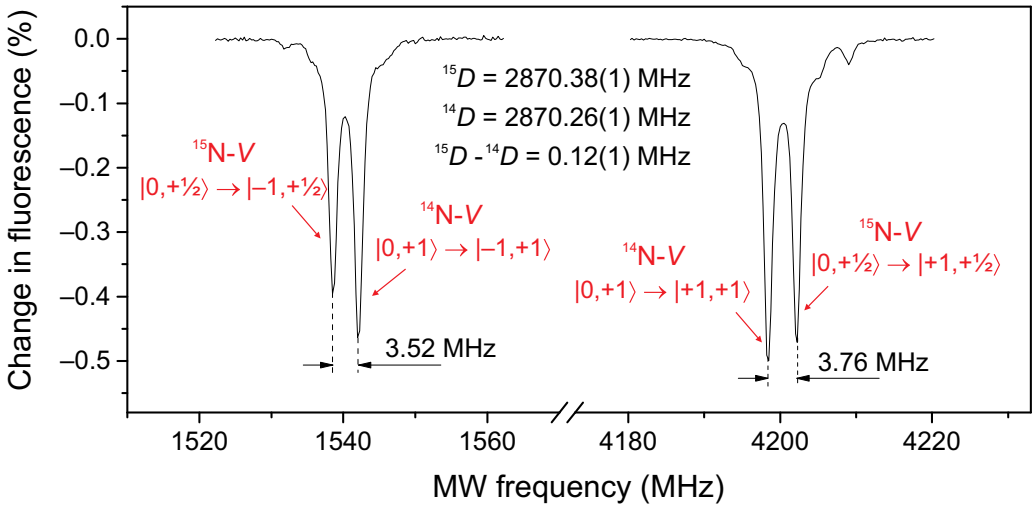

FIG. 7. Measurement of isotopic shift in D using ODMR. The spectrum is obtained from the G3 sample (50:50 isotopic ratio) at 475 G and consists of four resonances corresponding to two transitions (f_+, f_-) for ^{14}N-V and two transitions (f_+, f_-) for ^{15}N-V. At this field, the nuclear spins are optically polarized to their largest m_I sublevels, $m_I = +1$ for ^{14}N-V and $m_I = +1/2$ for ^{15}N-V, which creates a resolvable splitting. A slight difference is observed between the splitting of f_+ (3.76 MHz) and that of f_- (3.52 MHz), which corresponds to a difference in D of 0.12(1) MHz.

transverse magnetic fields (B_x) shift the nuclear-spin transition frequencies for both ^{14}N-V and ^{15}N-V. Terms in the Hamiltonian [Eq. (A1)] can be divided into terms that do ($H_\parallel$) and do not (V) commute with S_z and I_z:

$$H_\parallel = DS_z^2 + QI_z^2 + A_\parallel S_z I_z + \gamma_e B_z S_z - \gamma_n B_z I_z, \tag{C1}$$

$$V = \frac{A_\perp}{2}\left(S_+ I_- + S_- I_+\right) + \frac{\gamma_e B_x}{2}\left(S_+ + S_-\right). \tag{C2}$$

Here we have omitted the transverse nuclear-spin Zeeman term, which is small compared to the transverse electron-spin Zeeman term. Using $H_\parallel$ as the unperturbed Hamiltonian and treating V as a perturbation, the second-order perturbation shift of each unperturbed state is calculated using the following expression:

$$\Delta E^{(2)}_{m_s,m_I} = \sum_{m_s',m_I'} \frac{\left|\langle m_s', m_I'|\, V\,|m_s, m_I\rangle\right|^2}{E^{(0)}_{m_s,m_I} - E^{(0)}_{m_s',m_I'}}. \tag{C3}$$

Here the eigenstates of the unperturbed state are denoted as $|m_s, m_I\rangle$, and their energies are described as follows:

$$E^{(0)}_{m_s,m_I} = m_s^2 D + m_I^2 Q + m_s m_I A_\parallel + m_s \gamma_e B_z - m_I \gamma_n B_z. \tag{C4}$$

For each nuclear-spin transition, an approximate expression for the total energy shift is obtained to second order in $1/F_\pm$, where $F_\pm = D \pm \gamma_e B$. There are also fourth-order perturbation shifts that produce effects that are of second order in $1/F_\pm$, which appear when $m_s'' = m_s$ and $m_I'' \neq m_I$:

$$\Delta E^{(4)}_{m_s,m_I} = \sum_{m_s''',m_I'''} \sum_{m_I''\neq m_I} \sum_{m_s',m_I'} \frac{\langle m_s, m_I|\, V\,|m_s''', m_I'''\rangle\,\langle m_s''', m_I'''|\, V\,|m_s, m_I''\rangle\,\langle m_s, m_I''|\, V\,|m_s', m_I'\rangle\,\langle m_s', m_I'|\, V\,|m_s, m_I\rangle}{\left(E^{(0)}_{m_s,m_I} - E^{(0)}_{m_s''',m_I'''}\right)\left(E^{(0)}_{m_s,m_I} - E^{(0)}_{m_s,m_I''}\right)\left(E^{(0)}_{m_s,m_I} - E^{(0)}_{m_s',m_I'}\right)}, \tag{C5}$$

Combining these shifts gives us expressions for the shifted nuclear-spin transition frequencies, for both ^{14}N-V and ^{15}N-V:

$$f_1 = |Q| + {}^{14}\gamma_n B_z - \frac{A_\perp^2}{F_-} - A_\perp^2\left(\frac{|Q| - |A_\parallel|}{F_-^2} + \frac{2|Q| - |A_\parallel|}{F_+^2}\right) + \frac{\gamma_e^2 B_x^2}{2}\left[A_\perp^2 \frac{3}{Q}\left(\frac{1}{F_+} + \frac{1}{F_-}\right)^2 - |A_\parallel|\left(\frac{1}{F_-^2} - \frac{1}{F_+^2}\right)\right],$$

$$f_2 = |Q| - {}^{14}\gamma_n B_z - \frac{A_\perp^2}{F_+} - A_\perp^2\left(\frac{2|Q| - |A_\parallel|}{F_-^2} + \frac{|Q| - |A_\parallel|}{F_+^2}\right) + \frac{\gamma_e^2 B_x^2}{2}\left[A_\perp^2 \frac{3}{Q}\left(\frac{1}{F_+} + \frac{1}{F_-}\right)^2 + |A_\parallel|\left(\frac{1}{F_-^2} - \frac{1}{F_+^2}\right)\right],$$

$$
\begin{aligned}
f_3 &= |Q| - |A_\parallel| + {}^{14}\gamma_n B_z - A_\perp^2\left(\frac{2|Q| - |A_\parallel|}{F_-^2}\right) + \frac{\gamma_e^2 B_x^2}{2}\left[A_\perp^2\left(\frac{2}{Q - A_\parallel} + \frac{1}{Q + A_\parallel}\right)\frac{1}{F_-^2} + \frac{|A_\parallel|}{F_-^2}\right],\\
f_4 &= |Q| + |A_\parallel| - {}^{14}\gamma_n B_z + \frac{A_\perp^2}{F_-} - A_\perp^2\left(\frac{|Q|}{F_-^2}\right) + \frac{\gamma_e^2 B_x^2}{2}\left[A_\perp^2\left(\frac{1}{Q - A_\parallel} + \frac{2}{Q + A_\parallel}\right)\frac{1}{F_-^2} - \frac{|A_\parallel|}{F_-^2}\right],\\
f_5 &= |Q| + |A_\parallel| + {}^{14}\gamma_n B_z + \frac{A_\perp^2}{F_+} - A_\perp^2\left(\frac{|Q|}{F_+^2}\right) + \frac{\gamma_e^2 B_x^2}{2}\left[A_\perp^2\left(\frac{1}{Q - A_\parallel} + \frac{2}{Q + A_\parallel}\right)\frac{1}{F_+^2} - \frac{|A_\parallel|}{F_+^2}\right],\\
f_6 &= |Q| - |A_\parallel| - {}^{14}\gamma_n B_z - A_\perp^2\left(\frac{2|Q| - |A_\parallel|}{F_+^2}\right) + \frac{\gamma_e^2 B_x^2}{2}\left[A_\perp^2\left(\frac{2}{Q - A_\parallel} + \frac{1}{Q + A_\parallel}\right)\frac{1}{F_+^2} + \frac{|A_\parallel|}{F_+^2}\right],
\end{aligned}
\tag{C6}
$$

and

$$
\begin{aligned}
f_7 &= \left|{}^{15}\gamma_n\right| B_z + \frac{A_\perp^2}{2}\left(\frac{1}{F_-} - \frac{1}{F_+}\right) + \frac{A_\perp^2}{4}\left(\frac{A_\parallel}{F_-^2} - \frac{A_\parallel}{F_+^2}\right) + \frac{\gamma_e^2 B_x^2}{2}\left[\frac{A_\perp^2}{\left|{}^{15}\gamma_n\right| B_z}\left(\frac{1}{F_+} + \frac{1}{F_-}\right)^2 - A_\parallel\left(\frac{1}{F_-^2} - \frac{1}{F_+^2}\right)\right],\\
f_8 &= A_\parallel - \left|{}^{15}\gamma_n\right| B_z - \frac{A_\perp^2}{2}\left(\frac{1}{F_-}\right) - \frac{A_\perp^2}{4}\left(\frac{A_\parallel}{F_-^2}\right) + \frac{\gamma_e^2 B_x^2}{2}\left[\left(\frac{A_\perp^2}{A_\parallel} - A_\parallel\right)\frac{1}{F_-^2}\right],\\
f_9 &= A_\parallel + \left|{}^{15}\gamma_n\right| B_z - \frac{A_\perp^2}{2}\left(\frac{1}{F_+}\right) - \frac{A_\perp^2}{4}\left(\frac{A_\parallel}{F_+^2}\right) + \frac{\gamma_e^2 B_x^2}{2}\left[\left(\frac{A_\perp^2}{A_\parallel} - A_\parallel\right)\frac{1}{F_+^2}\right].
\end{aligned}
\tag{C7}
$$

These expressions can be reduced to obtain simplified expressions for the transition frequencies [see Eqs. (2) and (3)], as well as their angular dependences [see Eqs. (7) and (8)].

For ^{14}N-V, we can linearly combine nuclear-spin transition frequencies in order to obtain simple approximations for ${}^{14}\gamma_n B$, Q, and $A_\parallel$:

$$
\begin{aligned}
{}^{14}\gamma_n B &\approx \frac{f_3 - f_6}{2},\\
|Q| - |A_\parallel| &\approx \frac{f_3 + f_6}{2},\\
|Q| &\approx \frac{f_1 + f_2 + f_3 + f_4 + f_5 + f_6}{6},\\
|A_\parallel| &\approx \frac{f_1 + f_2 - 2f_3 + f_4 + f_5 - 2f_6}{6}.
\end{aligned}
\tag{C8}
$$

[1] C. L. Degen, F. Reinhard, and P. Cappellaro, Quantum sensing, Rev. Mod. Phys. **89**, 035002 (2017).

[2] M. P. Ledbetter, K. Jensen, R. Fischer, A. Jarmola, and D. Budker, Gyroscopes based on nitrogen-vacancy centers in diamond, Phys. Rev. A **86**, 052116 (2012).

[3] A. Ajoy and P. Cappellaro, Stable three-axis nuclear-spin gyroscope in diamond, Phys. Rev. A **86**, 062104 (2012).

[4] D. Maclaurin, M. W. Doherty, L. C. L. Hollenberg, and A. M. Martin, Measurable Quantum Geometric Phase from a Rotating Single Spin, Phys. Rev. Lett. **108**, 240403 (2012).

[5] T. W. Kornack, R. K. Ghosh, and M. V. Romalis, Nuclear Spin Gyroscope Based on an Atomic Comagnetometer, Phys. Rev. Lett. **95**, 230801 (2005).

[6] E. A. Donley and J. Kitching, in *Optical Magnetometry*, edited by D. Budker and D. F. Jackson Kimball (Cambridge University Press, Cambridge, 2013), p. 369.

[7] T. G. Walker and M. S. Larsen, in *Advances in Atomic, Molecular, and Optical Physics*, Vol. 65 (Academic Press, New York, 2016), p. 373.

[8] M. E. Limes, D. Sheng, and M. V. Romalis, ^{3}He–^{129}Xe Comagnetometry Using ^{87}Rb Detection and Decoupling, Phys. Rev. Lett. **120**, 033401 (2018).

[9] D. A. Thrasher, S. S. Sorensen, J. Weber, M. Bulatowicz, A. Korver, M. Larsen, and T. G. Walker, Continuous comagnetometry using transversely polarized Xe isotopes, Phys. Rev. A **100**, 061403 (2019).

[10] S. S. Sorensen, D. A. Thrasher, and T. G. Walker, A synchronous spin-exchange optically pumped NMR-gyroscope, Appl. Sci. **10**, 7099 (2020).

[11] V. M. Acosta, E. Bauch, M. P. Ledbetter, A. Waxman, L.-S. Bouchard, and D. Budker, Temperature Dependence of the Nitrogen-Vacancy Magnetic Resonance in Diamond, Phys. Rev. Lett. **104**, 070801 (2010).

[12] A. Jarmola, I. Fescenko, V. M. Acosta, M. W. Doherty, F. K. Fatemi, T. Ivanov, D. Budker, and V. S. Malinovsky, Robust optical readout and characterization of nuclear spin transitions in nitrogen-vacancy ensembles in diamond, Phys. Rev. Res. **2**, 023094 (2020).

[13] M. W. Doherty, V. M. Acosta, A. Jarmola, M. S. J. Barson, N. B. Manson, D. Budker, and L. C. L. Hollenberg, Temperature shifts of the resonances of the N-V^- center in diamond, Phys. Rev. B **90**, 041201 (2014).

[14] B. Bürgler, T. F. Sjolander, O. Brinza, A. Tallaire, J. Achard, and P. Maletinsky, All-optical nuclear quantum sensing using nitrogen-vacancy centers in diamond, npj Quantum Inf. **9**, 56 (2023).

[15] M. W. Doherty, N. B. Manson, P. Delaney, F. Jelezko, J. Wrachtrup, and L. C. Hollenberg, The nitrogen-vacancy colour centre in diamond, Phys. Rep. **528**, 1 (2013).

[16] S. Felton, A. M. Edmonds, M. E. Newton, P. M. Martineau, D. Fisher, D. J. Twitchen, and J. M. Baker, Hyperfine interaction in the ground state of the negatively charged nitrogen vacancy center in diamond, Phys. Rev. B **79**, 075203 (2009).

[17] A. Jarmola, S. Lourette, V. M. Acosta, A. G. Birdwell, P. Blümler, D. Budker, T. Ivanov, and V. S. Malinovsky, Demonstration of diamond nuclear spin gyroscope, Sci. Adv. **7**, eabl3840 (2021).

[18] V. V. Soshenko, S. V. Bolshedvorskii, O. Rubinas, V. N. Sorokin, A. N. Smolyaninov, V. V. Vorobyov, and A. V. Akimov, Nuclear Spin Gyroscope Based on the Nitrogen Vacancy Center in Diamond, Phys. Rev. Lett. **126**, 197702 (2021).

[19] P.-H. Chu, N. Ristoff, J. Smits, N. Jackson, Y. J. Kim, I. Savukov, and V. M. Acosta, Proposal for the search for new spin interactions at the micrometer scale using diamond quantum sensors, Phys. Rev. Res. **4**, 023162 (2022).

[20] J. F. Barry, J. M. Schloss, E. Bauch, M. J. Turner, C. A. Hart, L. M. Pham, and R. L. Walsworth, Sensitivity optimization for NV-diamond magnetometry, Rev. Mod. Phys. **92**, 015004 (2020).

[21] V. Jacques, P. Neumann, J. Beck, M. Markham, D. Twitchen, J. Meijer, F. Kaiser, G. Balasubramanian, F. Jelezko, and J. Wrachtrup, Dynamic Polarization of Single Nuclear Spins by Optical Pumping of Nitrogen-Vacancy Color Centers in Diamond at Room Temperature, Phys. Rev. Lett. **102**, 057403 (2009).

[22] B. Smeltzer, J. McIntyre, and L. Childress, Robust control of individual nuclear spins in diamond, Phys. Rev. A **80**, 050302 (2009).

[23] M. Steiner, P. Neumann, J. Beck, F. Jelezko, and J. Wrachtrup, Universal enhancement of the optical readout fidelity of single electron spins at nitrogen-vacancy centers in diamond, Phys. Rev. B **81**, 035205 (2010).

[24] M. Chen, M. Hirose, and P. Cappellaro, Measurement of transverse hyperfine interaction by forbidden transitions, Phys. Rev. B **92**, 020101 (2015).

[25] X.-D. Chen, C.-H. Dong, F.-W. Sun, C.-L. Zou, J.-M. Cui, Z.-F. Han, and G.-C. Guo, Temperature dependent energy level shifts of nitrogen-vacancy centers in diamond, Appl. Phys. Lett. **99**, 161903 (2011).

[26] S. Xu, M. Liu, T. Xie, Z. Zhao, Q. Shi, P. Yu, C.-K. Duan, F. Shi, and J. Du, Temperature-dependent behaviors of single spin defects in solids determined with Hz-level precision, arXiv:2212.02849 (2022).

[27] V. V. Soshenko, V. V. Vorobyov, S. V. Bolshedvorskii, O. Rubinas, I. Cojocaru, B. Kudlatsky, A. I. Zeleneev, V. N. Sorokin, A. N. Smolyaninov, and A. V. Akimov, Temperature drift rate for nuclear terms of the NV-center ground-state Hamiltonian, Phys. Rev. B **102**, 125133 (2020).

[28] G. Wang, A. R. Barr, H. Tang, M. Chen, C. Li, H. Xu, J. Li, and P. Cappellaro, Characterizing temperature and strain variations with qubit ensembles for their robust coherence protection, arXiv:2205.02790 (2022).

[29] H. Tang, A. R. Barr, G. Wang, P. Cappellaro, and J. Li, First-principles calculation of the temperature-dependent transition energies in spin defects, J. Phys. Chem. Lett. **14**, 3266 (2023).

[30] T. Umeda, K. Watanabe, H. Hara, H. Sumiya, S. Onoda, A. Uedono, I. Chuprina, P. Siyushev, F. Jelezko, J. Wrachtrup, and J. Isoya, Negatively charged boron vacancy center in diamond, Phys. Rev. B **105**, 165201 (2022).

[31] T. Xie, Z. Zhao, M. Guo, M. Wang, F. Shi, and J. Du, Identity Test of Single NV^- Centers in Diamond at Hz-Precision Level, Phys. Rev. Lett. **127**, 053601 (2021).

[32] A. Antušek, K. Jackowski, M. Jaszuński, W. Makulski, and M. Wilczek, Nuclear magnetic dipole moments from NMR spectra, Chem. Phys. Lett. **411**, 111 (2005).

[33] M. S. J. Barson, P. Reddy, S. Yang, N. B. Manson, J. Wrachtrup, and M. W. Doherty, Temperature dependence of the ^{13}C hyperfine structure of the negatively charged nitrogen-vacancy center in diamond, Phys. Rev. B **99**, 094101 (2019).